Similarity of Deep Continental Cumulus Convection as Revealed by a Three-Dimensional Cloud-Resolving Model

Marat F. Khairoutdinov and David A. Randall

Department of Atmospheric Science, Colorado State University, Fort Collins, Colorado

ABSTRACT

A three-dimensional cloud-resolving simulation of midlatitude continental convection during the Atmospheric Radiation Measurement (ARM) program summer 1997 intensive observation period (IOP) is used to study the similarity of several second and third statistical moments, and second-moment budgets among five episodes of deep convection. Several parameter scales relevant to deep convection similarity are introduced. The dimensionless vertical profiles of the vertical velocity variance and its third moment, cumulus kinetic energy, the prognostic variables' variances and fluxes, their budgets, as well as several triple correlations cluster together, confirming the dynamical similarity of the simulated convective events.

The dimensionless budgets of several second-order moments, such as convective kinetic energy (CKE), its vertical and horizontal components, variance, and vertical fluxes of the prognostic thermodynamic variables, as well as the momentum flux, are also presented. The most interesting aspect of the simulated CKE budget is that, in contrast to the boundary layer and shallow trade wind cumulus convection, the dissipation term is relatively small compared to the dominant buoyancy production, transport, and pressure correlation terms. The prognostic equation for the bulk CKE, defined as the vertically integrated mean CKE per unit area, is also discussed. It is found that the so-called bulk CKE dissipation timescale ranges in the simulation from 4 to 8 h. Therefore, the bulk CKE, mostly contained in the horizontal branches of mesoscale circulations associated with the deep convective systems, can persist much longer than the lifetime of an individual convective cloud. It is also found that the fraction of the bulk CKE associated with the vertical motions is about the same for all of the events considered, suggesting a strong correlation between the bulk CKE and the strength of the convective updrafts. It is shown that the bulk CKE dissipation timescale is inversely proportional to the square root of the bulk CKE itself. It is also found that the convective velocity scale is closely related to the convective available potential energy (CAPE) of the thermodynamic sounding taken immediately before a particular convective event.

1. Introduction

A cloud-resolving model (CRM), sometimes also called a cloud ensemble model, is a model that resolves most of the heat and water transport associated with convective clouds developing in response to the external forcing, for a simulated time period much longer than a life cycle of individual clouds, and in a domain large enough to contain many convective clouds. Although the so-called large eddy simulation (LES) models can also be viewed as CRMs when applied to a cloudy planetary boundary layer (PBL) or shallow trade-wind cumuli, the term CRM is usually reserved for models of deep cumulus convection.

The main focus of LES studies has always been on statistical–dynamical properties of boundary layer turbulence rather than on particular realizations of turbulence. Dynamical similarity of various convective PBL regimes, from the surface-driven dry mixed layers (e.g., Deardorff 1974; Moeng 1984) to radiatively driven stratocumulus-topped PBLs (e.g., Deardorff 1980; Moeng 1986; Stevens et al. 1998), has been shown using the so-called convective scales that have made it possible to collapse the multitude of the PBL dynamical and thermodynamical characteristics into a smaller number of dimensionless parameters and universal functions.

The main interest of CRM studies has been on interactions among convective clouds, large-scale circulation, and radiation, with the goal to evaluate and, ultimately, to improve the cloud parameterizations used in general circulation models (GCMs) and mesoscale models (e.g., Gregory and Miller 1989; Xu and Krueger 1991; Xu et al. 1992; Randall et al. 1996). Consequently, the statistical properties of deep convection derived from CRM simulations have almost exclusively been limited to mean vertical profiles of convective mass fluxes, heating and moistening rates, as well as water, energy, and momentum budgets, primarily because those profiles could be compared in a rather straightforward manner to the output produced by single-column versions of GCMs subjected to similar forcing.

Corresponding author address: Dr. Marat F. Khairoutdinov, Dept. of Atmospheric Science, Colorado State University, Fort Collins, CO 80523.
E-mail: marat@atmos.colostate.edu

To our knowledge, there has been no systematic attempt to apply the methodology developed by the LES community to CRM simulations of deep cumulus convection. In particular, there have been no CRM studies of the dynamical similarity of the statistical properties of deep convection and the associated budgets of second moments such as kinetic energy, momentum fluxes, scalar fluxes, and variances. Such detailed information could be useful not only to add to our general understanding of how deep convection works, but also for further progress and new ideas in parameterization of convection in large-scale models. Among the observational studies, the dynamical similarity of deep convection was probably first investigated by Zipser and LeMone (1980) who looked at the similarity of the ratio of mean updraft core velocity to the maximum possible velocity, and who also compared the dimensionless observed vertical profile of the vertical velocity in deep convective cores to analogous profiles obtained for boundary layer plumes.

In this paper, statistical information is derived for several convective events over the United States Great Plains as simulated by our three-dimensional CRM. Section 2 briefly describes the model and the simulation used in this study. Despite rather large differences in the large-scale forcing, precipitation rates, and vigor, as discussed in section 3, the convection during these events was dynamically similar. This is shown by using several appropriate convective scales as described in section 4. Several dimensionless second-moment budgets are presented in section 5, while section 6 shows the third-moment profiles in relation to the corresponding second moments. Section 7 describes some bulk properties of simulated deep convection. This is followed by a summary and conclusions in section 8.

2. Model and simulation setup

A detailed description of the CRM is given in Khairoutdinov and Randall (2001, manuscript submitted to *J. Atmos. Sci.*, hereafter KR). The equations of motion are written using the anelastic approximation. The prognostic thermodynamic variables are the liquid/ice water static energy $h_L = c_p T + gz - L_c(q_c + q_r) - L_s(q_i + q_s + q_g)$, the total nonprecipitating water $q_T = q_v + q_c + q_i$ (water vapor + cloud water + cloud ice), and the total precipitating water $q_p = q_r + q_s + q_g$ (rain + snow + graupel). Here, T is the temperature; g is the gravitational acceleration; c_p is the specific heat at constant pressure; and L_c and L_s are the latent heat of evaporation and sublimation, respectively. Note that inclusion of the precipitating water into the definition of h_L allows one to implicitly account for melting and freezing when precipitating water is represented by one prognostic variable. The partitioning of the cloud condensate and precipitating water into the liquid and ice phases is assumed to be a function of temperature only, with the hydrometeor conversion rates expressed similarly to the bulk microphysics scheme of Lin et al. (1983). The subgrid-scale model employs a 1.5-order closure based on a prognostic subgrid-scale turbulent kinetic energy or a simple Smagorinsky-type closure. The latter is used in this study. The advection of momentum is computed with the second-order finite differences in flux form with kinetic energy conservation. The equations of motion are integrated using the third-order Adams–Bashforth scheme with a variable time step. All prognostic scalar variables are advected using the fully three-dimensional positive definite and monotonic scheme of Smolarkiewicz and Grabowski (1990). The surface fluxes are computed using Monin–Obukhov similarity. A three-dimensional domain has $128 \times 128 \times 64$ grid points with 2-km horizontal resolution and variable vertical resolution gradually increasing from 100 m near the surface to 500 m above 5 km. The domain uses periodic lateral boundaries with the top at 27 km. The time step is 10 s.

The results of this study are based on a 28-day-long simulation using the large-scale forcing derived from observations made during the Atmospheric Radiation Measurement (ARM) program summer 1997 intensive observation period (IOP) campaign over the ARM Southern Great Plains (SGP) site in Oklahoma and Nebraska (Zhang et al. 2001). The forcing data include the large-scale temperature and water vapor advective tendencies as well as the surface latent and sensible heat fluxes. Since the large-scale pressure gradient is not available, the domain averaged wind is relaxed toward the observed profiles using a 6-h relaxation timescale. The radiative heating rate is prescribed from the estimates by the European Centre for Medium-Range Weather Forecasts (ECMWF) model.

The choice of the domain size and resolution was mostly constrained by relatively high computational cost of prolonged three-dimensional simulations. In a separate study (KR), using much shorter (4 day) simulations, we found that quadrupling the horizontal domain size from the domain size used in this study had virtually no effect on the simulated convective statistics. The grid resolution was a greater concern, especially in the context of this study, since the perturbation statistics derived from the three-dimensional fields are computed using the resolved information. A similar problem exists in LES studies of the boundary layer turbulence; however, it is generally accepted that as long as the bulk of the advective transport is resolved, the perturbation statistics derived from the resolved fields should be robust. Fortunately, in this study, less than 10% of simulated fluxes associated with deep cumulus convection were subgrid-scale and, therefore, parameterized, with the exception of a thin layer near the surface where the vertical transport was mostly due to subgrid-scale diffusion.

3. Convective events

As demonstrated by the time series of simulated hourly mean precipitation rate shown in Fig. 1, a few rather
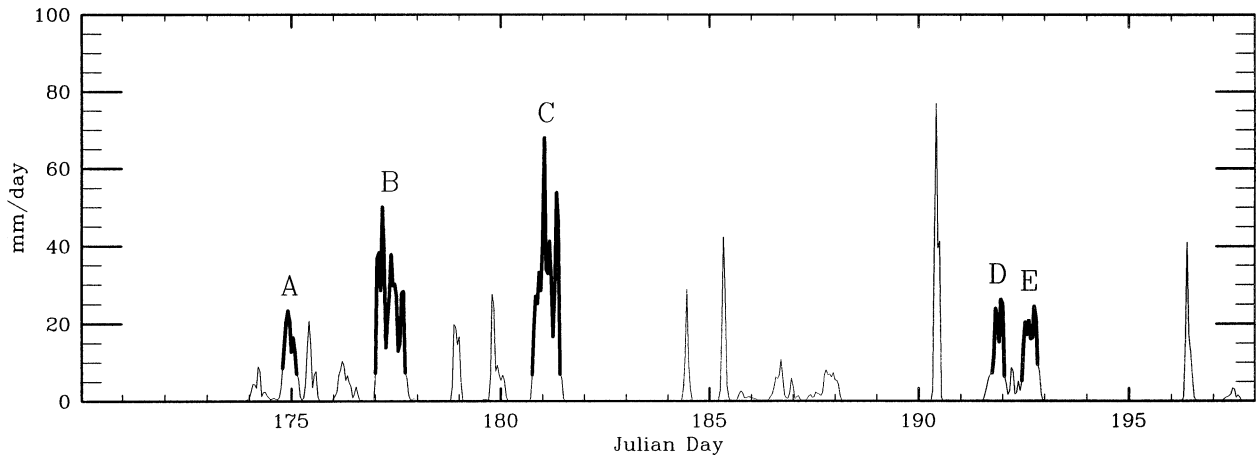
Fig. 1. Time series of simulated hourly precipitation rate. The subperiods corresponding to the convective events used in this study are highlighted by thick lines.

strong episodes of deep convection occurred during the simulated 28-day period. For this study, we identified five subperiods or convective events that produced hourly precipitation rates in excess of 10 mm day^{-1} for at least 5 consecutive hours (Table 1). The events were from 5 to 15 h long, with the event-mean precipitation rates in the range from 17 to 35 mm day^{-1}.

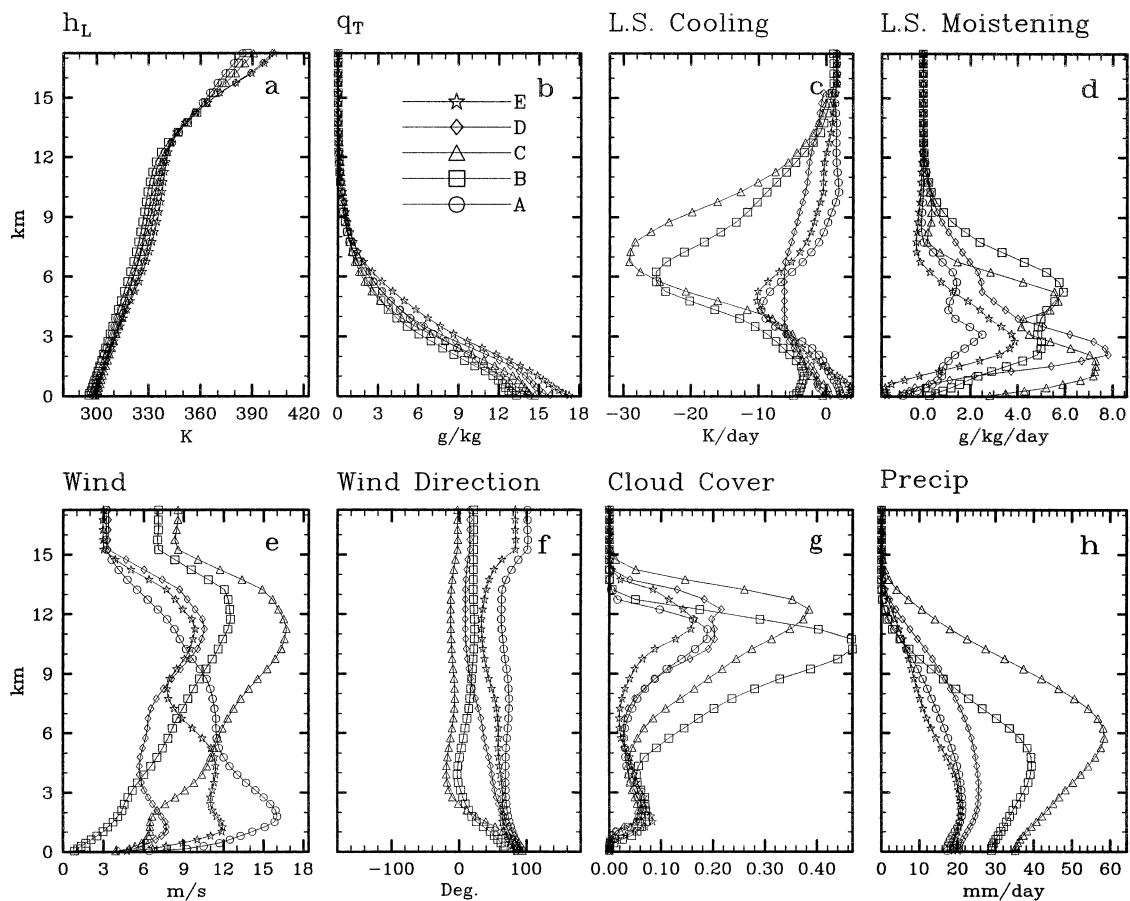Figure 2 shows the vertical profiles of some of the

Fig. 2. Profiles of the (a) liquid/ice water static energy, (b) total nonprecipitating water content, large-scale advective (c) cooling and (d) moistening tendencies, mean wind's (e) amplitude and (f) direction (counterclockwise from the west–east direction), (g) cloud fraction, and (h) precipitation flux for different convective events.

TABLE 1. Convective events used in the study (also see Fig. 1).

Event	A	B	C	D	E
Duration, (h)	6	15	14	5	7
Start (Julian day UTC)	174.833	177.042	180.792	191.792	192.500
End (Julian day UTC)	175.083	177.667	181.375	192.000	192.792
Mean precipitation (mm day^{-1})	17.3	28.9	35.1	20.7	18.9

properties of the environment, large-scale forcing, and mean cloud statistics averaged over each of the convective events. One can see that, although the domain-averaged profiles of h_L (Fig. 2a) and q_T (Fig. 2b) do not vary much for the considered events, the large-scale advective cooling (Fig. 2c) and moistening (Fig. 2d) tendencies, and the magnitude and direction of the vertical wind shear (Fig. 2e and Fig. 2f), differ rather significantly. These differences in the forcing result in rather large quantitative differences in the vertical distribution of simulated cloud cover fraction (Fig. 2g) and precipitation flux (Fig. 2h). The momentum flux profiles are also quite different (Fig. 3), which is not surprising considering the differences among the corresponding wind-component profiles (Figs. 3a and 3b). Overall, the momentum fluxes tend to be downgradient, producing, in some cases, rather substantial drag on the mean wind field.

Several important dynamical characteristics are shown in Fig. 4. As is well known, a virtual potential temperature flux $\overline{w'\theta_v'}$, also called a buoyancy[1] flux, plays a dominant role in the production of the convective kinetic energy. It is positive in the boundary layer as the result of positive surface sensible and latent heat fluxes; it becomes slightly negative just above the boundary layer; then it turns positive again in the region of free convection where most of the kinetic energy is generated; finally, it becomes negative due to updrafts

[1] In addition to virtual effects, the definition of the buoyancy in the model also includes the water loading.

penetrating above the level of neutral buoyancy. The minimum flux tends to be at about the same level as the local maximum of the mean cloud fraction (Fig. 2g) and mean cumulus kinetic energy (CKE; Fig. 4d). The CKE is defined as $\overline{e} \equiv 0.5\overline{\rho}(\overline{u'^2} + \overline{v'^2} + \overline{w'^2})$, where u, v, and w are the Cartesian components of the wind velocity; the overbar represents the horizontal average; and the prime represents a perturbation from that average. Note that this definition differs from the definition of the turbulent kinetic energy (TKE) commonly used in PBL studies, by incorporating the air density factor. The vertical velocity variance (Fig. 4b) and third moment (Fig. 4c) vary among the events by factors of 5 and 8, respectively. The liquid water/ice static energy flux $\overline{w'h_L'}$ (Fig. 4e) and the total nonprecipitating water flux $\overline{w'q_T'}$ (Fig. 4f) are mostly downgradient, and vary by factors of 4 and 5, respectively. The variances of both prognostic scalars $\overline{h_L'^2}$ (Fig. 4g) and $\overline{q_T'^2}$ (Fig. 4h) show local maxima in the boundary layer; $\overline{h_L'^2}$ has the largest maximum in the anvil layer. In two cases, $\overline{q_T'^2}$ has a secondary maximum just above the boundary layer.

4. Convective scales and similarity

Dynamic similarity among the simulated convective events will now be demonstrated using appropriate scaling parameters. The height will be scaled by z_* defined as the height at which the buoyancy flux near the cloud top is most negative. As was mentioned in the previous section, this height approximately coincides with the cloud fraction maximum near the cloud
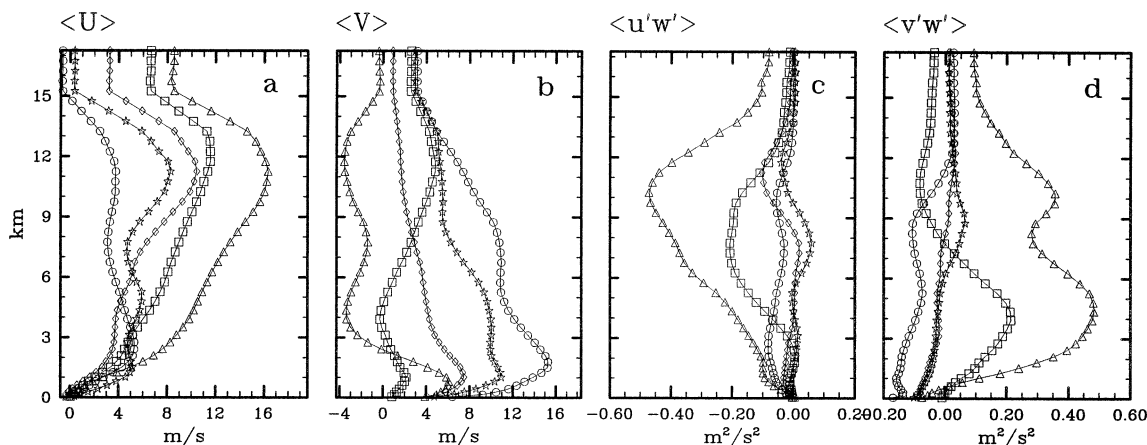

FIG. 3. Profiles of the (a) west–east and (b) south–north wind components and their (c), (d) corresponding fluxes for different convective events.

TABLE 2. Convective scales for the convective events in Table 1.

Event	A	B	C	D	E
z_*(m)	11 750	11 250	12 750	12 750	12 750
w_*(m s^{-1}) [see (1)]	2.20	2.98	4.49	2.91	2.07
ρ_*(kg m^{-3}) [see (2)]	0.55	0.58	0.53	0.55	0.54
T_*(K) [see (3)]	0.167	0.199	0.280	0.166	0.137
q_*($\times\ 10^{-3}$ kg kg^{-1}) [see (4)]	0.062	0.081	0.108	0.071	0.055

top; therefore, it can be a proper measure of the vertical extent of a convective system. The convective velocity scale w_* is based on the vertically integrated buoyancy flux following Deardorff (1980), who introduced this scale for the convective stratocumulus-topped boundary layers. Because the kinetic energy is proportional to air density, we modified Deardorff's original definition to include the nonnegligible variation of air density with height:

$$w_*^3 = 2.5 \frac{g}{\Theta \rho_*} \int_0^{z_*} \overline{\rho w' \theta_v'}\ dz. \tag{1}$$

Here, Θ is the mean tropospheric temperature, and ρ_* is the air density scale defined as

$$\rho_* = \frac{1}{z_*} \int_0^{z_*} \overline{\rho}\ dz. \tag{2}$$

Finally, the thermodynamic scales T_* and q_* for h_L and q_T, respectively, are defined using the vertical integrals of the corresponding fluxes $\overline{w'h_L'}$ and $\overline{w'q_T'}$ as

$$T_* = \frac{1}{c_p \rho_* w_* z_*} \int_0^{z_*} \overline{\rho w' h_L'}\ dz, \tag{3}$$

$$q_* = \frac{1}{\rho_* w_* z_*} \int_0^{z_*} \overline{\rho w' q_T'}\ dz. \tag{4}$$

The values of the scales (1)–(4) for different convective events are listed in Table 2. One can see that while the values of z_* varied only within 15% down from their maximum, and ρ_* even less, the other parameters varied by as much as a factor of 2. The simulated quantities can now be made dimensionless and plotted against the dimensionless height z/z_* as in Fig. 5, which is a dimensionless version of Fig. 4. One can see that there is quite a remarkable similarity among the simulated convective events in terms of the second-order moment statistics and the third moment of the vertical velocity.

The dimensionless buoyancy flux (Fig. 5a) has a rather thick layer of negative values near the top, with the thickness of about $0.35z_*$, presumably as a result of updrafts overshooting their levels of neutral buoyancy in the vicinity of $z = 0.85z_*$. The maxima of vertical velocity variance $\overline{w'^2}$ (Fig. 5b) and third moment $\overline{w'^3}$ (Fig. 5c) are about $0.13w_*^2$ and $0.4w_*^3$, respectively, and both occur at $z = 0.7z_*$. Above the PBL, the CKE (Fig. 5d) seems to maintain a nearly constant value of $1.2\rho_* w_*^2$, up to $z = z_*$. Profiles of the scalar fluxes

$\overline{w'h_L'}$ and $\overline{w'q_T'}$ have the extremes of about $-1.8c_p w_* T_*$ and $1.1w_* q_*$ at $z = 0.7z_*$ and $z = 0.3z_*$, respectively. The dimensionless profiles of liquid water static energy variance $\overline{h_L'^2}$ show considerable scatter among the events; they all have a sharp maximum near the surface, presumably as a result of the convective downdrafts; the largest maximum is located aloft, in the anvil layer, in the vicinity of $z = 0.9z_*$ where most of the detrainment seems to occur. The total nonprecipitating water variance $\overline{q_T'^2}$ also has a maximum near the surface; two events, D and E, have also secondary maxima in the vicinity of $z = 0.3z_*$. Note that the latter two cases also have the strongest vertical gradient of $\overline{q_T}$ above the PBL (see Fig. 2b), and, consequently, relatively large gradient-production rates of $\overline{q_T'^2}$ there, as shown in section 5c. Finally we note that convection is limited in the vertical by $z = 1.2z_*$.

5. Second-moment budgets

In this section, the budgets of several second moments are presented. The procedure that was used to compute the budget terms was not straightforward and simple. The direct evaluation of the budget terms using variable interpolation would inevitably produce rather large residuals of the budgets, because of the truncation errors of the finite-difference representation of the model equations on a staggered grid as was pointed out by Deardorff (1974). The budget terms in this study have been obtained by multiplying the computed tendencies of the prognostic variables, due to various terms of the corresponding prognostic equations, by an appropriate prognostic variable in a manner similar to the analytical derivations of the corresponding budget equations. Unfortunately, sometimes, only the sum of two budget terms can be evaluated directly by this method. For example, multiplication of the velocity advective tendencies in the momentum equations by the vertical velocity, and then summation over all three velocity components, produces a sum of two CKE budget terms: the advective transport term and the shear production term. The transport term is then computed using a simple interpolation method, while the shear production term is estimated as the residual. This procedure has drawbacks, a discussion of which is beyond the scope of this paper, but, in general, it virtually guarantees smallness of the computed budget residuals. The residual due to the storage term was generally small due to the aver-
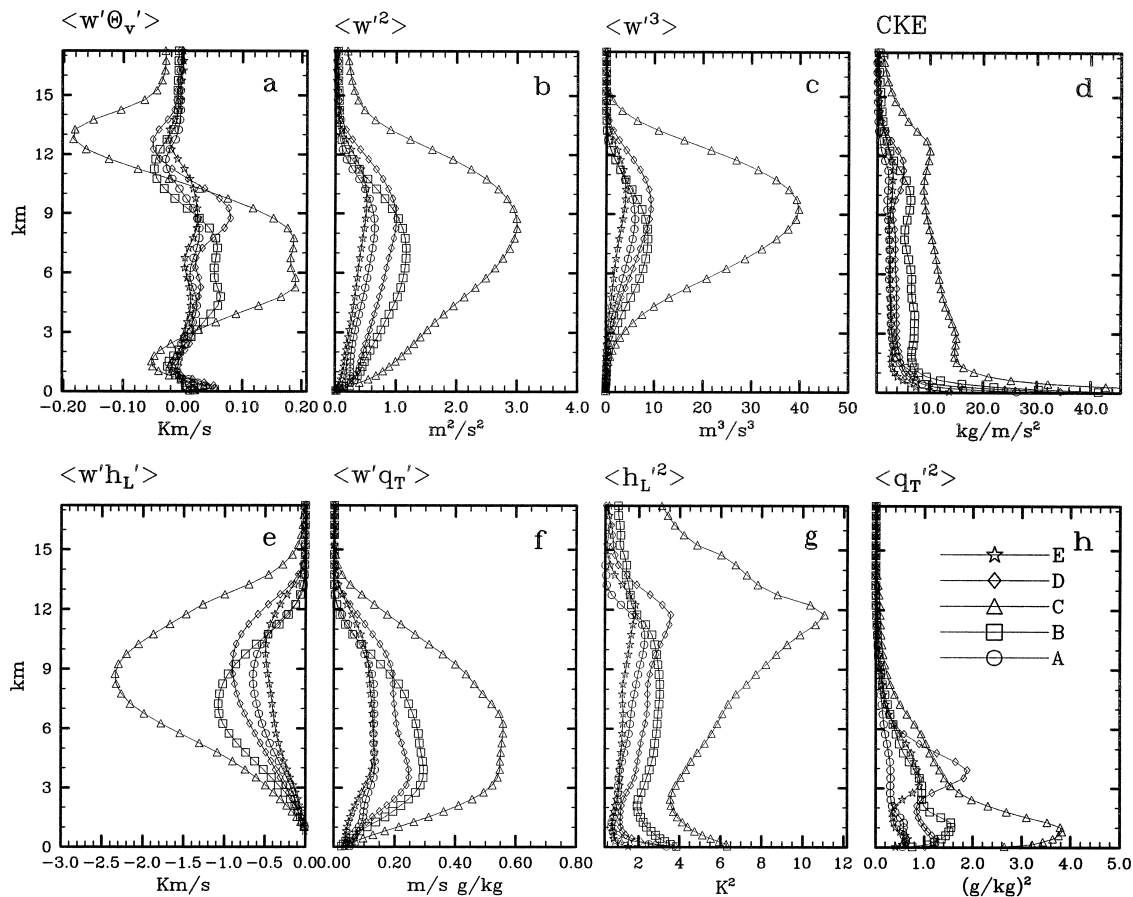
FIG. 4. Profiles of the (a) buoyancy flux, (b) vertical velocity variance, (c) vertical velocity's third moment, (d) cumulus kinetic energy, (e), (f) fluxes, and (g), (h) variances of the liquid/ice water static energy and total nonprecipitating water, respectively, for different convective events.

aging of the budgets over a period of many hours for each convective event.

a. Convective kinetic energy

A prognostic equation for the CKE is derived from the equations of motion in a manner similar to the procedure used in the derivation of the TKE equation (see, e.g., Stull 1988). Here, we present only the result, which, in its horizontally averaged form, can be written as follows:

$$\frac{\partial}{\partial t}\overline{e} = -\frac{\partial}{\partial z}\overline{w'e'} - \frac{\partial}{\partial z}\overline{w'p'} - \overline{\rho}\left(\overline{u'w'}\frac{\partial\overline{u}}{\partial z} + \overline{v'w'}\frac{\partial\overline{v}}{\partial z}\right)$$

$$\qquad T \qquad + \quad P \qquad + \qquad\qquad S$$

$$+ \ \overline{\rho}\beta\overline{w'\theta'_v} \ - \ \varepsilon. \qquad\qquad (5)$$

$$+ \qquad B \qquad + \ D.$$

The term denoted by T is the transport of CKE by the flow, P is the pressure correlation term, S represents the production of CKE by the mean vertical wind shear, B

is the buoyancy production term, and D is the viscous dissipation of CKE.[2]

The CKE budget terms, made dimensionless by $\rho_* w_*^3/z_*$, are shown in Fig. 6 as functions of z/z_*. These terms vary with the dimensionless height in a quite similar manner. One of the most interesting aspects of the simulated CKE budget is that above the PBL the buoyancy production, transport, and pressure correlation terms dominate, while the dissipation term is relatively small. Despite its relatively small amplitude, the domain-integrated CKE dissipation nearly balances the domain-integrated buoyancy production, as discussed further in section 7, because the transport and pressure correlation terms neither produce nor destroy the CKE but rather redistribute it vertically (their vertical integrals over the whole depth of the atmosphere are zero). It is the triple-moment transport term that brings the CKE generated in the middle layers up to the anvil region where it is mostly con-

---

[2] For physical interpretations of each term of the CKE equation and other budget equations used in this paper see, for example, Stull (1988).
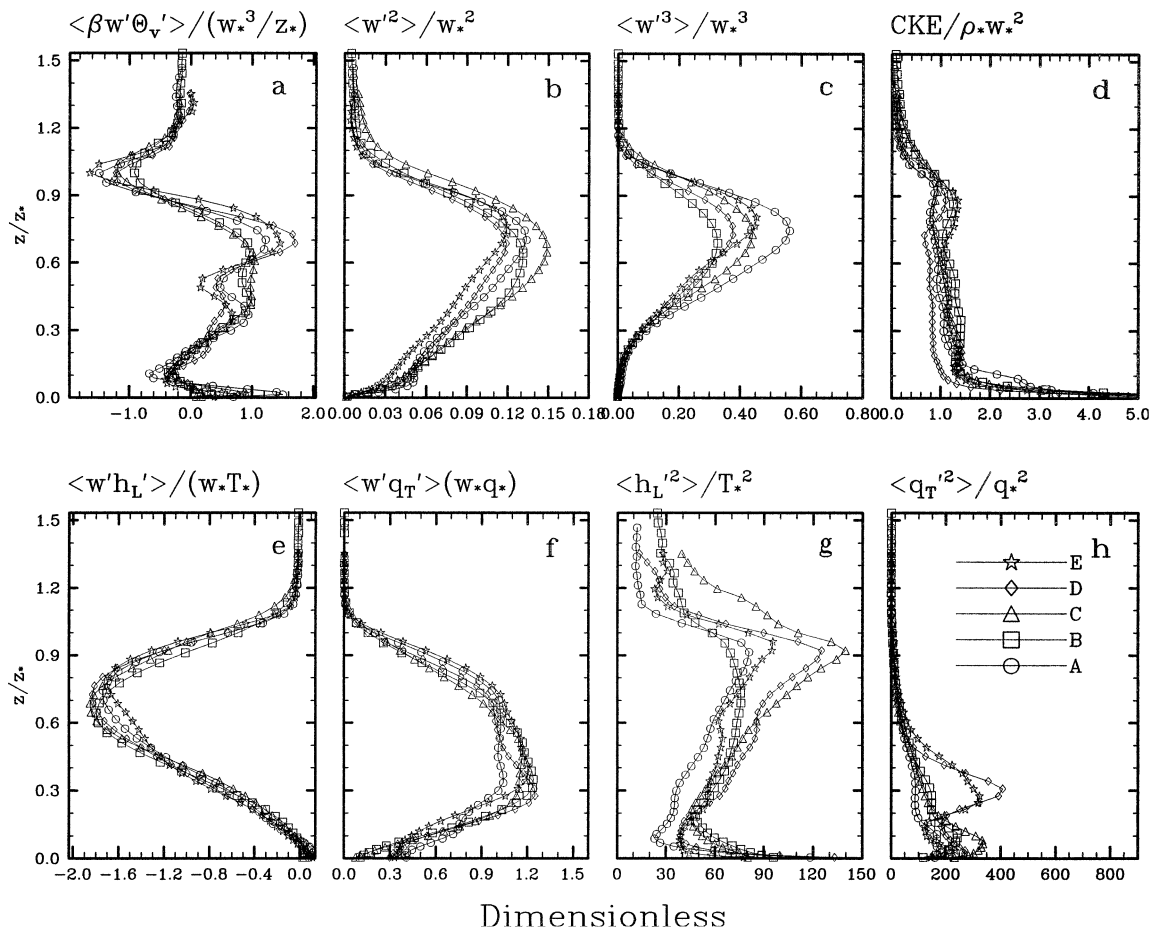
FIG. 5. Same as Fig. 4, but made dimensionless for each convective event using the convective scales (1)–(4).

sumed by the work against the buoyancy forces, presumably in the overshooting updrafts. The pressure correlation term generally works against the buoyancy production term to restore the hydrostatic balance disturbed by the vertical motions. Wind shear does not seem to play any important role in the CKE production above the PBL.

b. Horizontal and vertical velocity variance budgets

The CKE budget can be broken into its horizontal and vertical velocity components as

$$\frac{\partial}{\partial t}\overline{\rho}\frac{\overline{u'^2}+\overline{v'^2}}{2}$$

$$= -\frac{\partial}{\partial z}\overline{\rho}\overline{w'\frac{(u'^2+v'^2)}{2}} - \overline{\rho}\left(\overline{u'w'}\frac{\partial\overline{u}}{\partial z}+\overline{v'w'}\frac{\partial\overline{v}}{\partial z}\right)$$
$$\qquad T \qquad\qquad + \qquad\qquad S$$

$$- \frac{\overline{p'}}{\overline{\rho}}\frac{\partial\overline{\rho w'}}{\partial z} - \varepsilon_{uu},$$
$$+ \qquad R \qquad + \quad D$$
$$\tag{6}$$

$$\frac{\partial}{\partial t}\overline{\rho}\frac{\overline{w'^2}}{2}$$

$$= -\frac{\partial}{\partial z}\overline{\rho}\frac{\overline{w'^3}}{2} - \frac{\partial}{\partial z}\overline{w'p'} + \overline{\rho}\beta\overline{w'\theta'_v} + \frac{\overline{p'}}{\overline{\rho}}\frac{\partial\overline{\rho w'}}{\partial z} - \varepsilon_{ww},$$
$$\quad T \quad + \quad P \quad + \quad B \quad + \quad R \quad + \quad D$$
$$\tag{7}$$

where the term notation is similar to one used in the CKE budget equation; one additional symbol R denotes the pressure redistribution term. One can see in Figs. 7 and 8 that the horizontal velocity variance is produced by 1) conversion of the vertical motions into the horizontal motions through the pressure redistribution term,[3] and 2) shear production in the boundary layer. It is then transported to the anvil region by the updrafts. It is interesting that the pressure redistribution term by itself does not seem to play a dominant role in maintaining the horizontal velocity variance aloft; instead, the hor-

---

[3] Note that the pressure redistribution term has opposite signs in the horizontal and vertical variance budgets; therefore, CKE cannot be created or destroyed by that term.
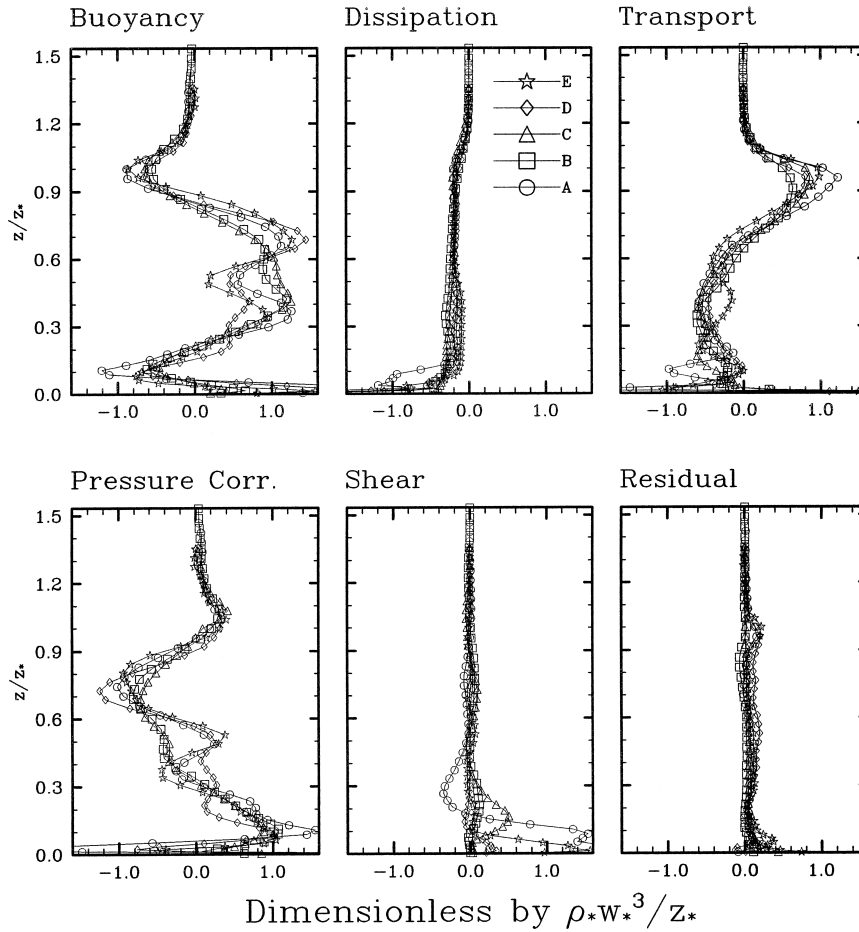
$0.5\,\rho\,(<u'^2> + <v'^2> + <w'^2>)$ Budget

FIG. 6. Dimensionless profiles of various terms of the CKE budget (5) for different convective events.
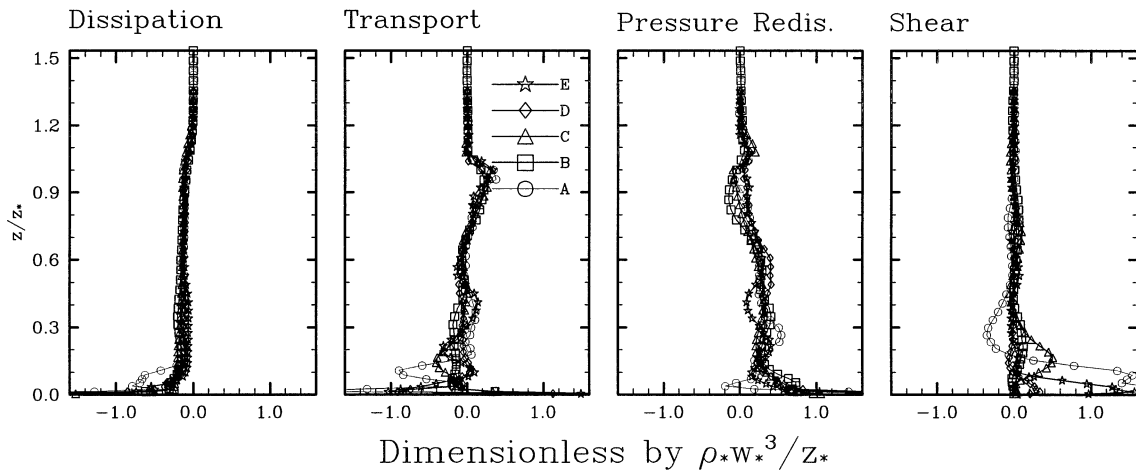
$0.5\,\rho\,<u'^2+v'^2>$ Budget

FIG. 7. Dimensionless profiles of various terms of the horizontal velocity variance budget (6) for different convective events.

izontal velocity variance there is mostly maintained by the mechanical transport of variance generated by the shear and pressure redistribution term in the lower troposphere. The vertical velocity variance budget closely resembles the CKE budget; for example, it is generated by the positively buoyant updrafts in the middle troposphere and then transported into the upper and lower troposphere to be consumed by the work against buoyancy forces.

c. Variance budgets for h_L and q_T

The prognostic equations for the h_L and q_T variances are derived by subtracting the horizontally averaged prognostic equations from their full versions (given in KR), and multiplying the result by the corresponding perturbation. The horizontally averaged equations are then written as follows:

$$\frac{\partial}{\partial t}\overline{h_L'^2}$$

$$= -\overline{\rho}^{-1}\frac{\partial}{\partial z}(\overline{\rho}\,\overline{w'h_L'^2}) - 2\overline{w'h_L'}\frac{\partial \overline{h_L}}{\partial z} - 2\overline{h_L'\frac{\partial}{\partial z}LP} - \varepsilon_{hh},$$
$$\qquad\quad T \qquad\qquad + \quad G \qquad + \quad PC \qquad + \; D$$
$$\tag{8}$$

$$\frac{\partial}{\partial t}\overline{q_T'^2}$$

$$= -\overline{\rho}^{-1}\frac{\partial}{\partial z}(\overline{\rho}\,\overline{w'q_T'^2}) - 2\overline{w'q_T'}\frac{\partial \overline{q_T}}{\partial z} + 2\overline{q_T'\left(\frac{\partial q_T}{\partial t}\right)_{\text{prec}}} - \varepsilon_{qq},$$
$$\qquad\quad T \qquad\qquad + \quad G \qquad + \quad PC \qquad + \; D$$
$$\tag{9}$$

where $LP \equiv L_cP_r + L_sP_s + L_sP_g$; and P_r, P_s, and P_g are the rain, snow, and graupel precipitation fluxes, respectively. The subscript ''prec'' represents the tendency of nonprecipitating water due to conversion to and evaporation of precipitating water. The terms denoted by T represent the transport by flow, G denotes the gradient production of variance by a variable's mean vertical gradient, PC represents the effect of precipitation, and D denotes dissipation of the variance due to the effects of diffusion.[4]

The budgets (8) and (9), made dimensionless by $w_*T_*^2/z_*$ and $w_*q_*^2/z_*$, are shown, respectively, in Figs. 9 and 10. One can see that the gradient production of the variances by the vertical motions is mostly offset by precipitation. As with the CKE budget, the molecular dissipation seems to play a small role in the scalar variance budget.

---

[4] The term with radiation production is omitted from Eq. (8), since the prescribed radiative cooling was applied uniformly at each model level.

d. Flux budgets for h_L and q_T

The prognostic equations for the mean vertical fluxes of h_L and q_T can be derived by multiplying a corresponding variable's perturbation equation by the vertical velocity perturbations, the vertical velocity equation by the variable's perturbations, and combining the results. The horizontally averaged budgets then read

$$\frac{\partial}{\partial t}\overline{w'h_L'} = -\frac{1}{\overline{\rho}}\frac{\partial}{\partial z}(\overline{\rho}\,\overline{w'w'h_L'}) - \overline{w'^2}\frac{\partial \overline{h_L}}{\partial z} + \beta\overline{h_L'\theta_v'}$$
$$\qquad\qquad\quad T \qquad\qquad + \quad G \qquad + \quad B$$

$$\qquad - \overline{h_L'\frac{\partial}{\partial z}\frac{p'}{\rho}} - \overline{w'\frac{\partial}{\partial z}LP},$$
$$\qquad + \quad P \quad + \quad PC$$
$$\tag{10}$$

$$\frac{\partial}{\partial t}\overline{w'q_T'} = -\frac{1}{\overline{\rho}}\frac{\partial}{\partial z}(\overline{\rho}\,\overline{w'w'q_T'}) - \overline{w'^2}\frac{\partial \overline{q_T}}{\partial z} + \beta\overline{q_T'\theta_v'}$$
$$\qquad\qquad\quad T \qquad\qquad + \quad G \qquad + \quad B$$

$$\qquad - \overline{q_T'\frac{\partial}{\partial z}\frac{p'}{\rho}} + \overline{w'\left(\frac{\partial q_T}{\partial t}\right)_{\text{prec}}},$$
$$\qquad + \quad P \quad + \quad PC$$
$$\tag{11}$$

where T is the transport of flux by the flow, G is the gradient production of flux due to a variable's mean vertical gradient, B is the buoyancy covariance production term, P is called the pressure-scalar covariance term, and PC represents the effects of precipitation.

The budgets (10) and (11), made dimensionless by $c_pT_*w_*^2/z_*$ and $q_*w_*^2/z_*$, are shown, respectively, in Figs. 11 and 12. Note that only the sum of the buoyancy and pressure-scalar correlation terms is shown. These terms are much bigger than the rest due to relatively large mesoscale perturbations of the temperature and water vapor fields in the cold pools formed by the convective outflow in the boundary layer and in the anvil. Despite their relatively large magnitudes, these terms tend to be in very close equilibrium because of the quasi-hydrostatic balance of the mesoscale perturbation pressure gradient and the perturbation buoyancy; therefore, only the deviation from that balance matters for maintaining the scalar fluxes. It appears that the combined buoyancy and pressure terms act to reduce the corresponding flux; a similar effect is exerted by the precipitation processes. Because the sign of the gradient production term is always opposite to that of a transported variable's vertical gradient, the vertical motions always increase the magnitudes of the fluxes of h_L and q_T.

e. Momentum flux budget

The momentum flux budget for the west–east wind components can be derived in the following form:

0.5 ρ $<w'^2>$ Budget
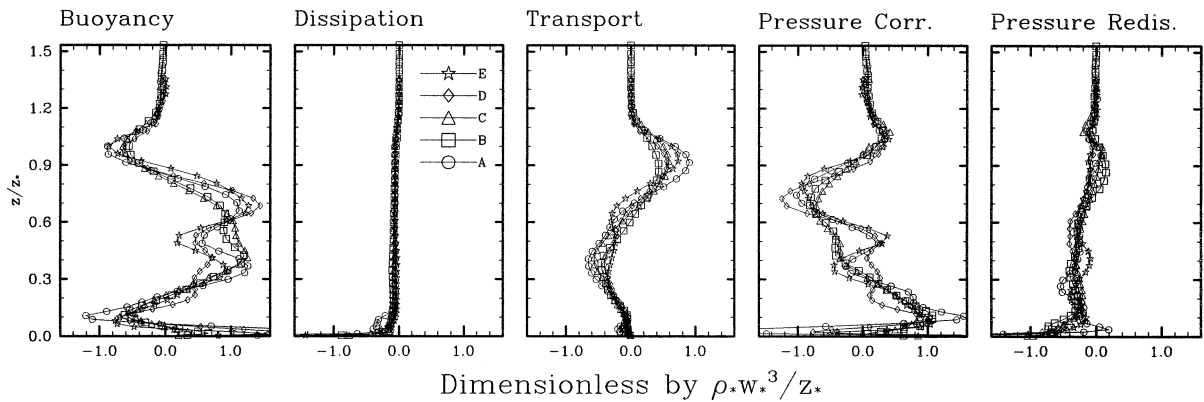

FIG. 8. Dimensionless profiles of various terms of the vertical velocity variance budget (7) for different convective events.

$$\frac{\partial}{\partial t}\overline{\rho u' w'} = -\frac{\partial}{\partial z}\overline{\rho w' w' u'} - \overline{\rho w'^2}\frac{\partial \overline{u}}{\partial z} + \overline{\rho}\beta\overline{u'\theta'_v}$$
$$\qquad\qquad T \qquad + \quad S \quad + \quad B$$

$$- \frac{\partial}{\partial z}\overline{u' p'} + \overline{\frac{p'}{\rho}\left(\frac{\partial\overline{\rho}w'}{\partial x} + \frac{\partial\overline{\rho}u'}{\partial z}\right)}, \qquad (12)$$
$$+ \quad P \quad + \qquad\qquad R$$

where T denotes the transport, S is the shear production of flux due to a variable's mean vertical gradient, B is the buoyancy covariance production term, P is the pressure correlation term, and R is the pressure anisotropy or "return-to-isotropy" term. The budget of the south–north wind component is written in a similar fashion and will not be discussed here. The budget terms are plotted in Fig. 13. As was the case with the scalar flux budgets, both pressure terms P and R and the buoyancy term B are about an order of magnitude larger than the other terms (especially in the boundary layer), and seem to be also in approximate balance with each other, so

that only a deviation from that balance affects the momentum flux. The combined effect of the pressure and buoyancy terms is to reduce the magnitude of the momentum flux mostly produced by the wind shear interaction with the convective updrafts and downdrafts as indicated by the shear production term.

6. Triple correlations

The second-moment budgets, presented above, express the transport terms as divergences of the corresponding fluxes of the second moments. These third statistical moments, or triple correlations, are shown in Fig. 14. In general, these moments have rather unique dimensionless profiles for different convective events. Note that the second-moment fluxes share their signs with the second moments themselves, but not necessarily with the second moments' vertical gradients. This behavior suggests that, in the case of simulated deep convection, the second-moment fluxes cannot be, in
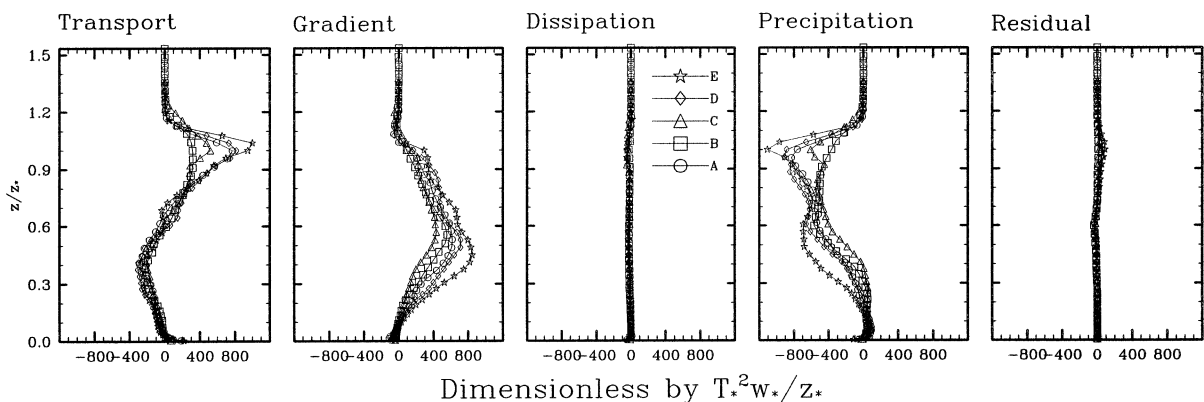
$<h_L'^2>$ Budget

FIG. 9. Dimensionless profiles of various terms of the liquid/ice water static energy variance budget (8) for different convective events.
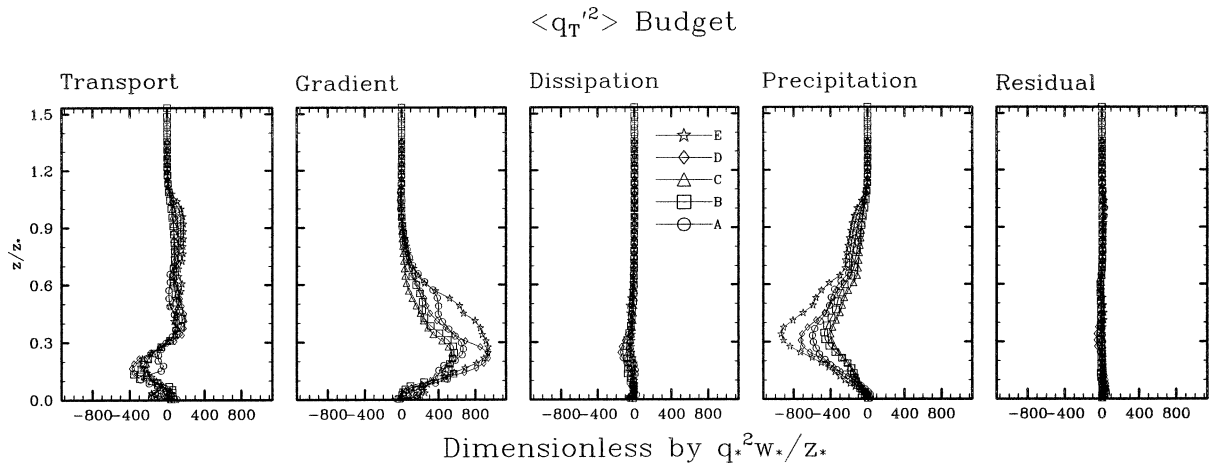
$<q_T'^2>$ Budget

FIG. 10. Dimensionless profiles of various terms of the total nonprecipitating variance budget (9) for different convective events.

general, parameterized as diffusion of the corresponding second moments, because this approximation requires downgradient transport. Instead, the shapes of the profiles for the second and the third moments suggest that it is perhaps better to assume "advection" rather than "diffusion," so that the second-moment fluxes are proportional to the second moments themselves as

$$\overline{\rho w' \varphi' \psi'} = \overline{\rho} W_{\varphi\psi} \overline{\varphi' \psi'}, \qquad (13)$$

where $W_{\varphi\psi}$ is some effective advection velocity. Figure 15 shows these velocities computed for each of the triple correlations in Fig. 14. Note that the velocities were computed when the second moments exceeded 5% of their maximum magnitudes within the convective layer. One can see that the velocities are indeed positive, suggesting the upward transport of the second moments by the convection. The shapes of the dimensionless profiles suggests that the advection velocity for the scalar-flux fluxes and for the vertical-velocity-variance flux (which is the vertical-momentum-flux flux) could be modeled

as linear with the dimensionless height, while the advection velocities for the scalar-variance fluxes and the CKE flux could be modeled as proportional to the vertical velocity variance, or, perhaps, its square root.

Note that there is a consistent difference of about a factor of 2 in the advection velocity between two groups of the convective events, with the first group including events B, C, and D, and the second group including events A and E. As seen in Fig. 2, the first group is characterized by positive wind shear (relatively light surface winds), and by rather large directional shear in the lower troposphere; the second group, on the other hand, has negative wind shear (relatively strong surface winds) and small directional shear. These factors may have affected the mesoscale organization of convective cells in the model. Perhaps, the triple correlations are particularly sensitive to even subtle changes in the convective statistics associated with different organizational patterns (e.g., squall lines vs super cells). We leave this topic for future investigation.
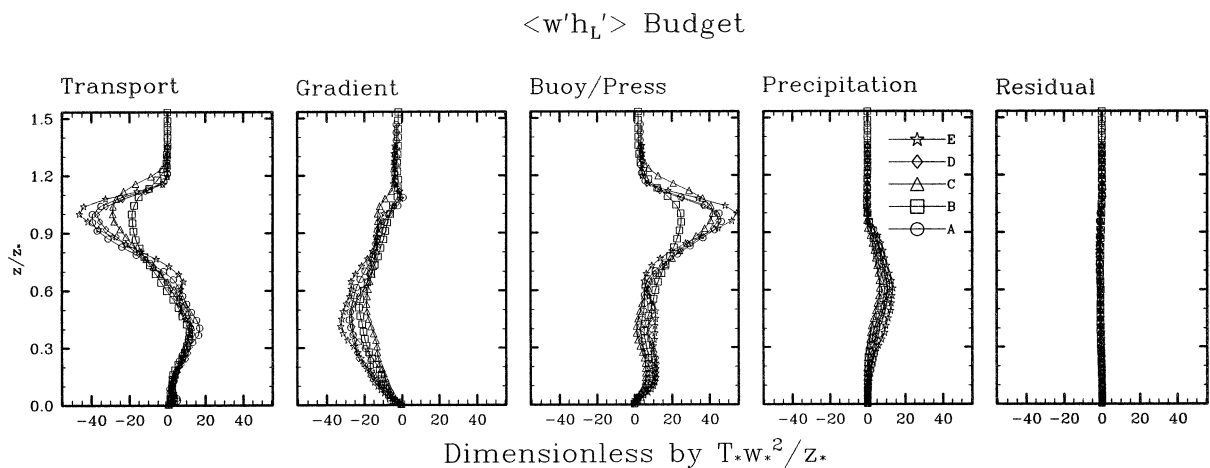
$<w'h_L'>$ Budget

FIG. 11. Dimensionless profiles of various terms of the liquid/ice water static energy flux budget (10) for different convective events.
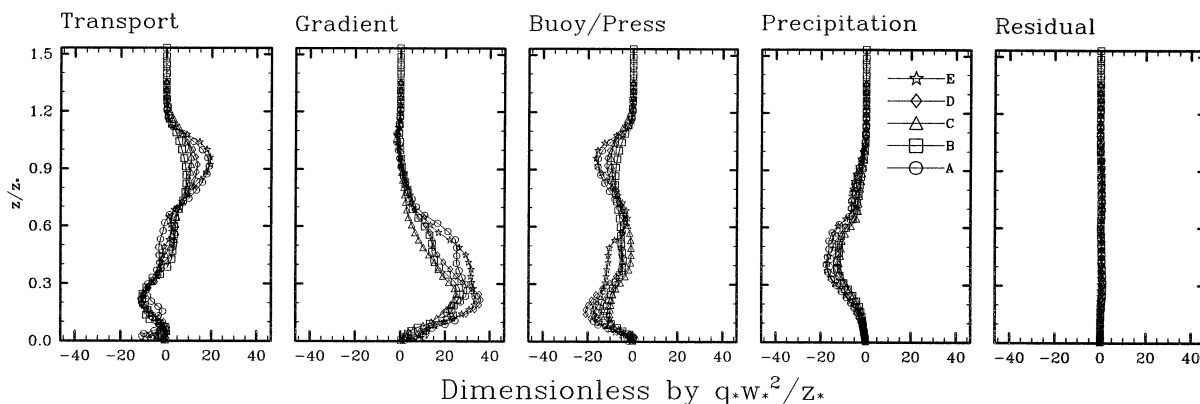
$<w'q_T'>$ Budget

FIG. 12. Dimensionless profiles of various terms of the total nonprecipitating water flux budget (11) for different convective events.

7. Bulk CKE budget and dissipation timescale

In this section, a balance of the vertically integrated or bulk CKE is discussed. A bulk CKE K is defined as

$$K = \int_0^{top} \overline{e} \, dz, \tag{14}$$

where "top" denotes the top of the domain. The prognostic equation for K is obtained by vertically integrating the CKE prognostic equation (5) over the depth of the domain. The result can be written in the following generic form:

$$\frac{\partial K}{\partial t} = B + S - D, \tag{15}$$

where B, S, and D denote the bulk CKE buoyant and shear production, and viscous dissipation, respective-

ly.[5] The values of these terms averaged over each convective event are given in Table 3. The bulk buoyancy production is in near balance with viscous dissipation, while shear production is not as significant. A rather large residual of the sum of these terms for some events may be explained by relatively short averaging intervals and therefore relatively large storage of K (note that the largest residual values correspond to the shortest events A, D, and C) as well as by the truncation and interpolation errors in the estimate of the CKE budget terms.

Equation (15) is similar to the equation used in the so-called prognostic mass-flux closure of Randall and

---

[5] Note that the vertically integrated transport and pressure correlation terms vanish since the vertical velocity is exactly zero at the surface and the top of the domain.
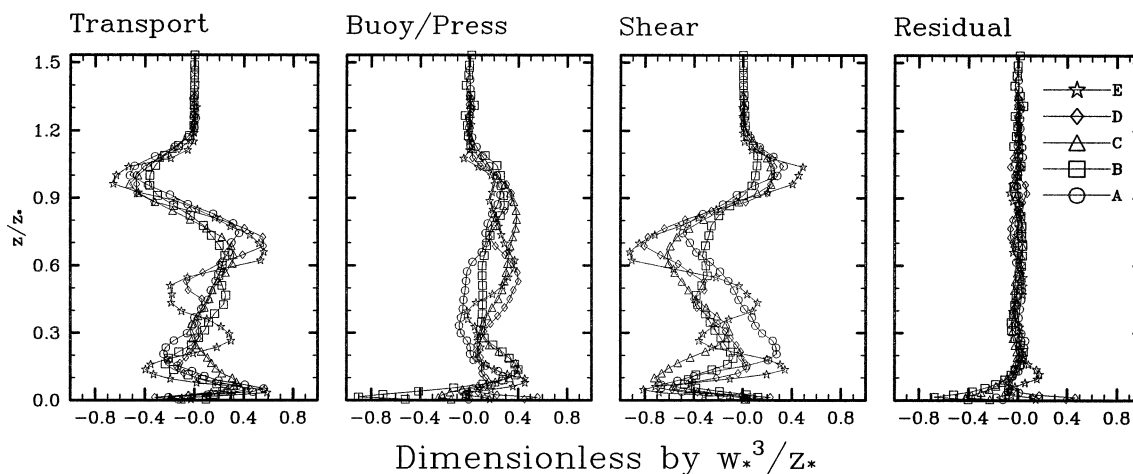
$\rho <w'u'>$ Budget

FIG. 13. Dimensionless profiles of various terms of the west–east momentum flux budget (12) for different convective events.
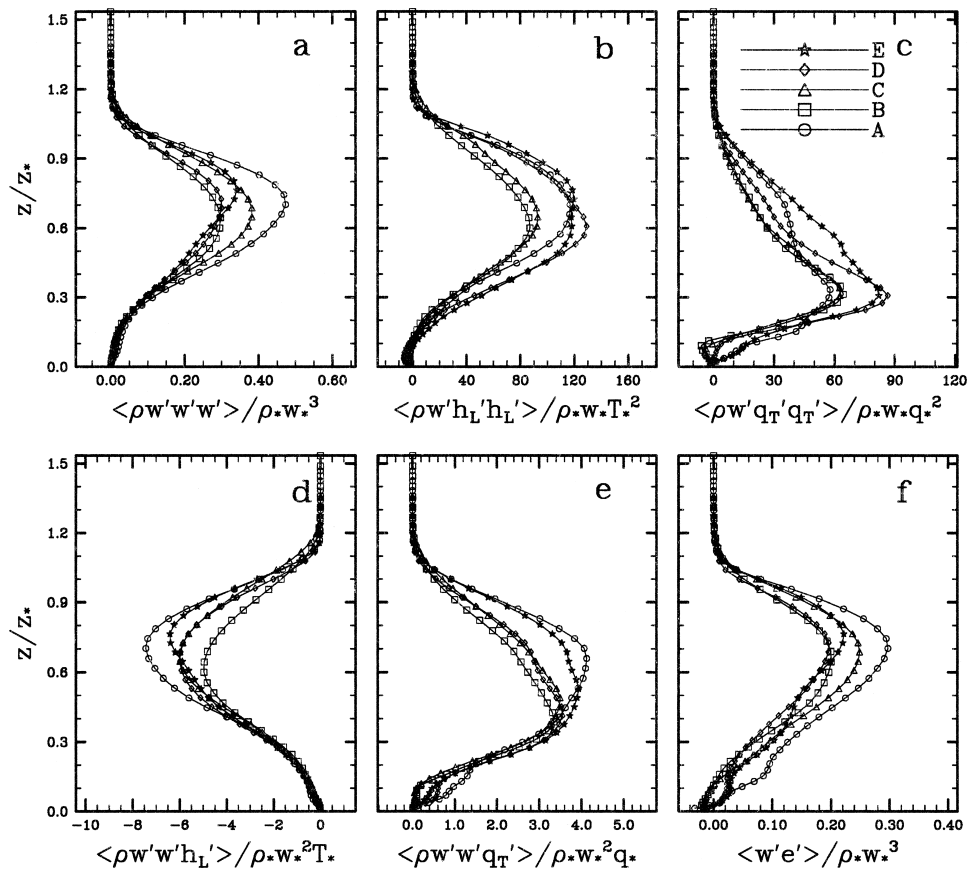
FIG. 14. Dimensionless profiles of the triple correlations from the second-moment-budget transport terms.

Pan (1993), which they applied to individual cloud types in their variant of the Arakawa–Schubert convective parameterization. They assumed a simple exponential-decay-like expression for the dissipation rate:

$$D = K/\tau_d, \tag{16}$$

where τ_d is the dissipation timescale, which they prescribed to be in the order of 10^3 s, arguing that it should not be larger than the lifetime of an individual cloud. We can compute τ_d directly; the results are given in Table 3. One can see that the bulk CKE dissipation timescale is about a factor of 4–5 larger than the "eddy overturning" timescale z_*/w_*. In dimensional units, τ_d varies in the range from 4 to more than 8 h, which is much longer than the lifetime of an individual convective cloud. In order to understand that rather unexpected result, we computed the fraction of the bulk CKE that is associated with the vertical motions only:

$$\mu = \frac{1}{2K} \int_0^{top} \overline{\rho} \overline{w'^2} \, dz. \tag{17}$$

One can see from the values of μ listed in Table 3 that less than 10% of the cumulus kinetic energy in the domain is associated with the convective updrafts and downdrafts; therefore, the CKE is mostly contained in the horizontal branches of the circulations, which is in

agreement with the findings by Xu et al. (1992). The circulation associated with a deep convective system apparently persists much longer than the lifetime of an individual convective cloud in that system. Note that the values of μ are nearly universal (consensus mean is 0.075), suggesting a strong correlation between the bulk CKE and the strength of the convective updrafts. This supports the assumption in the Randall–Pan closure that the CKE can be used to diagnose the updraft mass flux.

From the dimensional analysis, D can be expressed in an alternative form as

$$D = c\rho_*^{-1/2} z_*^{-3/2} K^{3/2}, \tag{18}$$

where c is some "universal" dimensionless constant. Note from values of c in Table 3 that indeed its range is rather narrow (consensus mean is 0.18), suggesting a universal nature of the expression (18). Comparing (16) and (18), we can express the dissipation timescale as

$$\tau_d = c_1 \rho_*^{1/2} z_*^{3/2} K^{-1/2}, \tag{19}$$

where $c_1 = 1/c$ (consensus mean is 5.5). For deep cumulus convection, the parameters ρ_* and z_* change in a rather narrow range (after all, the vertical extent of deep convection is limited by the depth of the tropo-
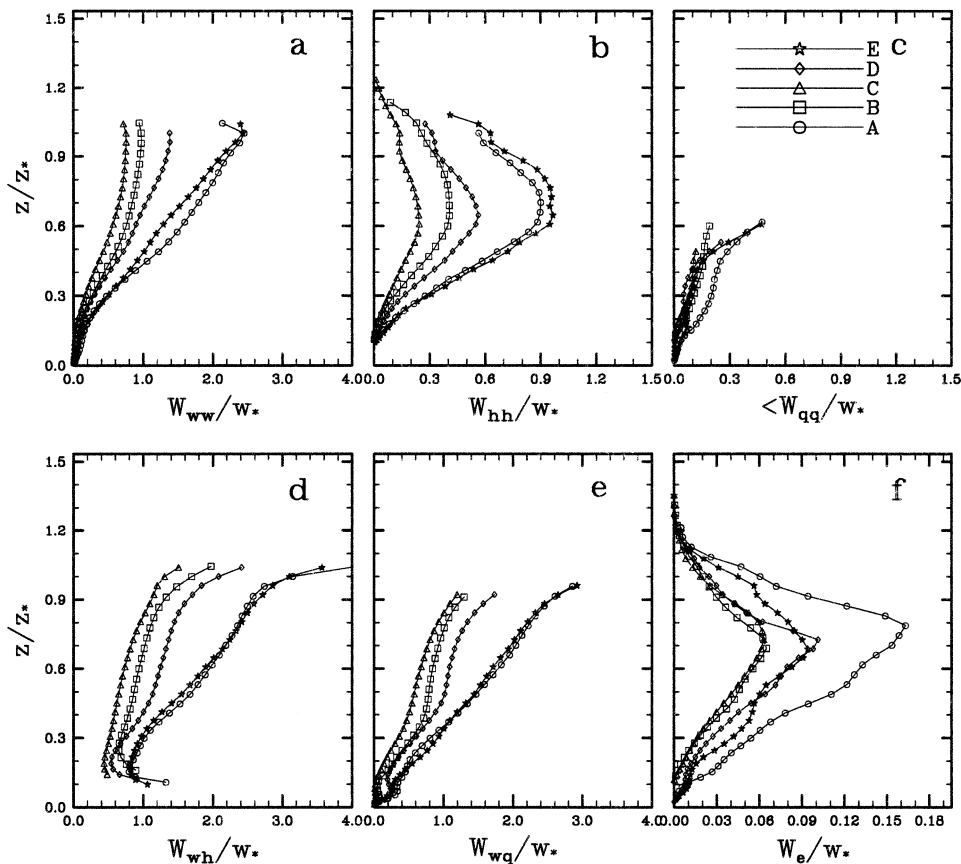
FIG. 15. Dimensionless profiles of the ratio of the triple correlations to the corresponding double correlations, or the effective advection velocity for the triple correlations in Fig. 14 (see the text for explanations).

sphere); therefore, the dissipation timescale depends almost entirely on a measure of the vigor of the convection, namely, K; specifically, it is inversely proportional to $\sqrt{K}$. Thus, the CKE dissipation timescale becomes shorter for more vigorous convective systems.

8. Velocity scale and CAPE

Another important issue is whether the convective available potential energy (CAPE) can be related to the velocity scale (1). The CAPE is a measure of the maximum velocity $w_c = [2(CAPE)]^{1/2}$ that a pseudoadiabatically lifted nonentraining parcel would achieve if

the CAPE was converted into the parcel's kinetic energy. The CAPE decreases rather rapidly as the result of convection; therefore, it has been computed for a simulated sounding taken right before a particular convective event. The values of CAPE, w_c, and the w_*/w_c ratio computed for each convective event are given in Table 4. While CAPE and corresponding w_c vary within factors of 4 and 2, respectively, the ratio w_*/w_c remains nearly constant (consensus mean is 0.063). Thus, in these particular instances of continental convection, the convective velocity scale w_* can, in fact, be directly computed from the CAPE of a sounding sampled right before a convective event: $w_* = c_2(CAPE)^{1/2}$, with consensus coefficient $c_2 = 0.089$.

As one can see from Table 3, the dimensionless bulk dissipation rate is rather robust, with a consensus value of 0.28. If we take the value for the density scale ρ_* as being 0.55, we can relate the bulk dissipation rate directly to CAPE in SI units as $D = 1.1 \times 10^{-4} (CAPE)^{3/2}$. It is estimated that the global dissipation rate from the energy transfer from the large scales to the smallest scales is about 2 W m^{-2} (Peixoto and Oort 1992); from the expression above we estimate that the corresponding value of CAPE would be about 700 J kg^{-1} if all of the dissipation was due to deep cumulus convection. This

TABLE 3. Various bulk statistics for the convective events in Table 1.

Event	A	B	C	D	E
$K/(\rho_* w_*^2 z_*)$ [see (14)]	1.29	1.49	1.49	1.05	1.22
$B/(\rho_* w_*^3)$ [see (15)]	0.33	0.31	0.31	0.39	0.33
$S/(\rho_* w_*^3)$ [see (15)]	0.12	0.01	0.04	0.00	0.1
$D/(\rho_* w_*^3)$ [see (15)]	0.32	0.27	0.30	0.24	0.25
τ_d (h)	6.0	5.8	3.9	5.3	8.3
$w_* \tau_d / z_*$	4.03	5.52	4.96	4.37	4.88
μ [see (17)]	0.072	0.072	0.076	0.080	0.073
c [see (18)]	0.21	0.15	0.16	0.22	0.18

TABLE 4. Convective available potential energy (CAPE) statistics.

Event	A	B	C	D	E
CAPE (J kg^{-1})	734	1267	2235	928	536
$w_c = (2$ CAPE$)^{1/2}$ (m s^{-1})	38.3	50.3	66.8	43.1	32.7
w_*/w_c	0.057	0.059	0.067	0.067	0.063

"typical" value of CAPE is rather similar to the observations (e.g., Williams and Rennó 1993) as well as theoretical estimates (e.g., Rennó and Ingersoll 1996; Emanuel and Bister 1996).

9. Summary and conclusions

In this study, we used the results of a three-dimensional cloud-resolving simulation of a midlatitude continental convection during the ARM summer 1997 IOP to show the similarity of several second and third statistical moments, as well as the second-moment budgets, among five episodes of deep convection using several convective scales similar to the scales used in LES studies of the cloud-topped PBLs. The dimensionless budgets of several second-order moments such as convective kinetic energy (CKE), its vertical and horizontal components, variance, and vertical flux of the prognostic thermodynamic variables, as well as momentum flux have also been presented.

The most interesting aspect of the simulated CKE budget is that, above the PBL, the dissipation term is relatively small compared to the dominant buoyancy production, transport, and pressure correlation terms. The large amount of CKE generated in the updraft cores is mostly removed aloft by the work against buoyancy forces at the cloud top, so that only a relatively small portion of the total CKE is actually dissipated. This makes the CKE budget in the case of deep convection differ from the CKE budget for the cloudy boundary layer and shallow trade wind convection, where the dissipation is a major player in the cloud layer itself, and the work done against the negative buoyancy forces is very small.

To illustrate this point, we conducted a simulation of shallow trade wind cumulus convection forced by the Barbados Oceanographic and Meteorological Experiment (BOMEX) data as used by the Global Energy and Water Cycle Experiment (GEWEX) Cloud System Studies (GCSS) Working Group 1 for their LES model intercomparison project (Siebesma et al. 2002, manuscript submitted to *J. Atmos. Sci.*). We utilized a version of the CRM that was identical to one used in this study of deep convection, but with a domain that had $128 \times 128 \times 75$ grid points and a uniform grid spacing of $\Delta x = \Delta y = 2.5\Delta z = 100$ m. The model was run for 6 h using a 2-s time step. Since there is no conventional way to identify the top of the trade wind cumulus convection, z_* was defined as the height at which the advective transport term reaches its local maximum, where, presumably, most of the detrainment takes place. The other

scales were defined using definitions (1)–(4). The scales were as follows: $z_* = 1540$ m, $w_* = 0.86$ m s^{-1}, $\rho_* = 1.1$ kg m^{-3}, $T_* = 0.017$ K, and $q_* = 0.058$ g kg^{-1}. These scales are very similar to those observed in the marine boundary layer, as presented by Lambert et al. (1999). Figure 16 shows the composite (averaged over all five events) dimensionless CKE budget for deep convection versus a corresponding dimensionless budget for the shallow convection averaged over the last three simulated hours. One can see that the viscous dissipation plays a dominant role in the dynamics of shallow convection; also, in contrast to the deep convection, the buoyancy flux for shallow convection remains strictly nonnegative except for a very shallow layer right at the top of the PBL.

The relative smallness of the dissipation rate in the case of deep convection may be a consequence of much wider deep convective cores and, presumably, smaller entrainment/detrainment rates per unit mass flux (e.g., de Roode et al. 2000). This notion is supported by larger contribution of the CKE transport term in the case of deep convection than in the case of shallow convection: 0.8 versus 0.5 $\rho_* w_*^3/z_*$ (see Fig. 16), which is similar to the relative magnitudes of dissipation rates: 0.2 versus 0.3 $\rho_* w_*^3/z_*$ (as pointed out by C. Bretherton 2002, personal communication).

The budgets for the variances of the prognostic scalars, which are the liquid/ice water static energy and the total water content, also have negligible molecular dissipation, while the dominant gradient production terms are mostly offset by the precipitation related terms. For the scalar and the momentum flux budgets, the pressure and buoyancy correlation terms are very large due to large mesoscale perturbations of temperature and water vapor fields in the boundary layer (cold pools) and in the anvil. However, these two terms tend to be in very close "quasi-hydrostatic" equilibrium with each other, so that only the deviation from that equilibrium (as expressed by their sum) affects the fluxes. In particular, the combined effect of these terms is to reduce the flux magnitude produced by the interaction of the vertical motions with the transported variable's vertical gradient (gradient production and shear production terms). Precipitation seems always to reduce the magnitude of the fluxes of the prognostic scalars.

We demonstrated that the triple correlations, such as the second-moment vertical fluxes, cannot be modeled as the diffusion of the second moments themselves, because of the upgradient transport over substantial depths of a convective layer. Instead, it is shown that the sec-
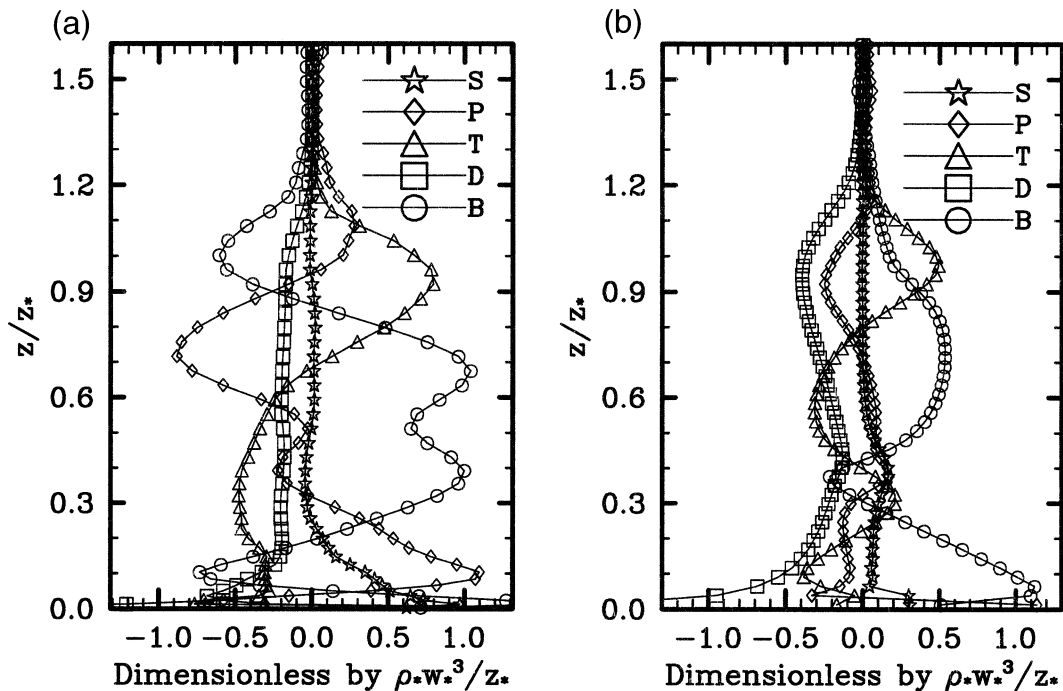
FIG. 16. The comparison of the CKE budgets for the (a) deep and (b) shallow convection. The deep convection budget is obtained by averaging the dimensionless CKE budgets for five ARM convective events. The shallow convection budget is obtained from the BOMEX trade wind cumulus convection simulation. Symbols are S for shear production, P for pressure correlation, T for transport, D for dissipation, and B for buoyancy production.

ond-moment fluxes can be modeled as an upward advection of the second moments themselves with an effective vertical velocity. The latter can be modeled as a linear function of the height in the case of the fluxes of fluxes, or as proportional to the vertical velocity variance (or its square root) in the case of scalar-variance fluxes.

We also discussed the prognostic equation for the bulk CKE, defined as the vertically integrated mean CKE per unit area. We showed that the so-called dissipation timescale that is usually chosen to be on the order of 1 h can actually range from 4 to more than 8 h for the convective events used in this study, which is much longer than the lifetime of an individual convective cell. Thus, the ratio of the bulk CKE dissipation timescale to the eddy overturning timescale z_*/w_* is a factor 4–5 in the case of deep convection. In contrast, a similarly defined ratio in the case of simulated BOMEX shallow convection is found to be close to one.

Our results also support the findings by Xu et al. (1992) that the most of the bulk CKE is contained in the horizontal branches of the circulation associated with deep convection. We found that the fraction of the bulk CKE associated with the vertical motions is about the same for all the considered events suggesting a strong correlation between the bulk CKE and the strength of the convective updrafts. This supports the assumption (used in the Randall–Pan prognostic clo-

sure) that the bulk CKE can be used to diagnose the updraft mass flux.

It has been shown, from dimensional arguments, that the bulk CKE dissipation timescale is inversely proportional to the square root of the bulk CKE itself; that is, the dissipation timescale is shorter for more vigorous convective events. We also found that the convective velocity scale can be uniquely estimated from the CAPE of the thermodynamic sounding taken right before the convective event.

We have to caution, however, that the results presented in this paper are based on a single simulation of one particular period of deep continental convection over the Southern Great Plains of the United States. Although the dynamical characteristics of several convective events that occurred during that particular period do appear to be quite similar, we do not suggest that the same similarity profiles would apply to any type of deep convection over wide variety of thermodynamic conditions and geographical locations. In fact, our preliminary analysis of simulated convection based on the Global Atmospheric Research Program (GARP) Atlantic Tropical Experiment (GATE) Phase III data shows a generally poor scalability of the dynamical characteristics using the convective scales introduced in this paper. The ARM convection events considered in this study represent the cases of explosive deep continental convection responding to very strong but brief forcing,

and dominated by a particular type of a deep convective system (a squall line, for example). The GATE convection represents tropical maritime convection modulated by the weakened African squall lines with almost continuous precipitation produced by an ensemble of various cloud types coexisting on a rather wide range of spatial and temporal scales. Therefore, it is rather difficult to extract a well defined convective event as we were easily able to do in the case of the ARM convection. The poor similarity of the simulated GATE convection may be due to "cross contamination" of the convective statistics by various convective types interacting in some complicated way. Each of those convective types, however, may still have dynamical similarity properties of its own. Future research may clarify this issue.

REFERENCES

Deardorff, J. W., 1974: Three-dimensional numerical study of turbulence in an entraining mixed layer. *Bound.-Layer Meteor.,* **7,** 199–226.

——, 1980: Stratocumulus-capped mixed layers derived from a three-dimensional model. *Bound.-Layer Meteor.,* **18,** 495–527.

de Roode, S. R., P. G. Duynkerke, and A. P. Siebesma, 2000: Analogies between mass-flux and Reynolds-averaged equations. *J. Atmos. Sci.,* **57,** 1585–1598.

Emanuel, K. A., and M. Bister, 1996: Moist convective velocity and buoyancy scales. *J. Atmos. Sci.,* **53,** 3276–3285.

Gregory, D., and M. J. Miller, 1989: A numerical study of the parameterization of deep tropical convection. *Quart. J. Roy. Meteor. Soc.,* **115,** 1209–1241.

Lambert, D., P. Durand, F. Thoumieux, B. Bénech, and A. Druilhet, 1999: The marine atmospheric boundary layer during SEMA-PHORE. II: Turbulence profiles in the mixed layer. *Quart. J. Roy. Meteor. Soc.,* **125,** 513–528.

Lin, Y.-L., R. D. Farley, and H. D. Orville, 1983: Bulk parameterization of the snow field in a cloud model. *J. Climate Appl. Meteor.,* **22,** 1065–1092.

Moeng, C.-H., 1984: A large-eddy simulation model for the study of planetary boundary layer turbulence. *J. Atmos. Sci.,* **41,** 2052–2062.

——, 1986: Large-eddy simulation of a stratus-topped boundary layer. Part I: Structure and budgets. *J. Atmos. Sci.,* **43,** 2886–2900.

Peixoto, J. P., and A. H. Oort, 1992: *Physics of Climate.* American Institute of Physics, 520 pp.

Randall, D. A., and D.-M. Pan, 1993: Implementation of the Arakawa–Schubert cumulus parameterization with a prognostic closure. *The Representation of Cumulus Convection in Numerical Models, Meteor. Monogr.,* No. 46, Amer. Meteor. Soc., 137–144.

——, K.-M. Xu, R. J. C. Somerville, and S. Iacobellis, 1996: Single-column models and cloud ensemble model as links between observations and climate models. *J. Climate,* **9,** 1683–1697.

Rennó, N. O., and A. P. Ingersoll, 1996: Natural convection as a heat engine: A theory for CAPE. *J. Atmos. Sci.,* **53,** 572–585.

Smolarkiewicz, P. K., and W. W. Grabowski, 1990: The multi-dimensional positive definite advection transport algorithm: Nonoscillatory option. *J. Comput. Phys.,* **86,** 355–375.

Stevens, B., W. R. Cotton, G. Feingold, and C.-H. Moeng, 1998: Large-eddy simulations of strongly precipitating, shallow, stratocumulus-topped boundary layers. *J. Atmos. Sci.,* **55,** 3616–3638.

Stull, R. B., 1988: *An Introduction to Boundary Layer Meteorology.* Kluwer Academic, 670 pp.

Williams, E. R., and N. O. Rennó, 1993: An analysis of the conditional instability of the tropical atmosphere. *Mon. Wea. Rev.,* **121,** 21–36.

Xu, K.-M., and S. K. Krueger, 1991: Evaluation of cloudiness parameterization using cumulus ensemble model. *Mon. Wea. Rev.,* **119,** 342–367.

——, A. Arakawa, and S. K. Krueger, 1992: The macroscopic behavior of cumulus ensembles simulated by a cumulus ensemble model. *J. Atmos. Sci.,* **49,** 2402–2420.

Zhang, M.-H., J. L. Lin, R. T. Cederwall, J. J. Yio, and S. C. Xie, 2001: Objective analysis of ARM IOP data: Method and sensitivity. *Mon. Wea. Rev.,* **129,** 295–311.

Zipser, E. J., and M. A. LeMone, 1980: Cumulonimbus vertical velocity events in GATE. Part II: Synthesis and model core structure. *J. Atmos. Sci.,* **37,** 2458–2469.